

Optical Engineering

SPIDigitalLibrary.org/oe

Extended high-angular-frequency analysis of turbulence effects on short-exposure imaging

David H. Tofsted

Extended high-angular-frequency analysis of turbulence effects on short-exposure imaging

David H. Tofsted*

U.S. Army Research Laboratory, Computational and Information Sciences Directorate, Attn: RDRL-CIE-D, White Sands Missile Range, New Mexico 88002-5501

Abstract. An improved analysis of optical turbulence effects on short-exposure passive (SE) imaging is described, resulting in a new analytic expression for the SE modulation transfer function (MTF). This analysis expands on a 2011 study that examined characteristics of a tilt-phase component discovered in the standard theory of SE turbulence effects characterization. The analysis introduces an improved integration technique and a reformulated phase structure function, facilitating computation of a 38,007 element database of MTF results at low- to high-angular frequencies covering a wide range of diffraction and turbulence conditions. Analysis of this database is described, yielding a new analytic SE MTF, accurate to a root-mean-square error of 0.000218 versus the database. Comparisons show that the new expression is well correlated to an alternative computationally intensive method, and it is a factor 29 to 64 improvement over prior analytic expressions. Limits of applicability of the approach for incoherent imaging are also discussed. The low-computational cost of the new method is suitable for systems performance modeling of turbulence impacts, including path-varying turbulence scenarios. © The Authors. Published by SPIE under a Creative Commons Attribution 3.0 Unported License. Distribution or reproduction of this work in whole or in part requires full attribution of the original publication, including its DOI. [DOI: [10.1117/1.OE.53.4.044112](https://doi.org/10.1117/1.OE.53.4.044112)]

Keywords: atmospheric optics; atmospheric turbulence; image formation theory; modulation transfer function.

Paper 131713 received Nov. 7, 2013; revised manuscript received Mar. 19, 2014; accepted for publication Mar. 20, 2014; published online Apr. 25, 2014.

1 Introduction

The problem of imaging in the presence of degrading optical turbulence conditions has been an ongoing area of active research for many years. Much recent research has focused on correcting imagery through image processing (dewarping and/or deconvolution) techniques.¹⁻⁸ Paralleling this inverse problem is the direct simulation of turbulence on clear images to create artificially degraded imagery at known turbulence levels⁹⁻¹² for benchmarking purposes. A third research area involves system intercomparisons for cost-effectiveness evaluation.¹³⁻¹⁵ In each case, undergirding the research is the core issue of establishing the baseline effect of turbulence on image quality, particularly for short-exposure (SE) imaging.

The standard method used by systems performance modelers¹³⁻¹⁷ had been Fried's SE modulation transfer function (MTF).¹⁸⁻²⁰ For example, Holst¹⁵ devotes an entire chapter to Fried's SE MTF. This model was the common choice due to its simplicity, despite the existence of more accurate (and numerically intensive) techniques (e.g., Ref. 21).

Critics of Fried's approach pointed to its high-frequency response failure when modeling high turbulence degradation influences.²¹⁻²³ Nonetheless, the simplicity of Fried's result suggested a re-examination of Fried's approach might yield new findings. The resulting study²⁴ examined the properties of an overlooked tilt-phase correlation term and developed improved expressions for diffraction influences on the turbulent phase structure function (PSF), angle-of-arrival variance, and therefore on the SE MTF. However, the numerical integration technique used was not optimal for evaluating the tilt-phase influence at combined high-angular frequency

and high-turbulence conditions. Consequently, a modeling compromise was adopted based on Fried's quadratic correction to the long-exposure (LE) MTF. This approach was subsequently critiqued by Charnotskii²⁵⁻²⁸ who argued its quadratic term would produce inaccurate results at high frequency.

This issue is addressed here through a new analysis of high-frequency turbulence effects and development of a new SE MTF analytic model. The new model exhibits diffraction-limited behavior at all frequencies while applying to a wider range of optical scenarios. The resulting model is compared with published calculations from a path-integral technique²¹ and a Markov method.²⁶ The model's Rytov approximation (RA)²⁹ is also described, and criteria developed by Tatarski²⁹ and Dashen³⁰ are examined to determine the extent of validity of modeled conditions.

The remainder of the paper is designed as follows: Section 2 describes the propagation model used, its justification, and numerical processing techniques developed to handle high-turbulence conditions. Section 3 describes the analysis process used to translate the computed database into the new analytical SE MTF expression. Section 4 presents comparisons with alternative approaches, followed by conclusions in Sec. 5.

2 Propagation and Imaging Models

The propagation model used is based on the Rytov approximation,^{16,29} involving a multiplicative turbulent scattering effect, using the imaging geometry of Fig. 1. Monochromatic incoherent light of wavelength λ emerges from the transverse object plane at $z = -L$. Photons pass through the system aperture's lens at $z = 0$ to reach the imaging plane at $z = R$. The system's thin lens optics are considered focused

*Address all correspondence to: David H. Tofsted, david.h.tofsted.civ@mail.mil

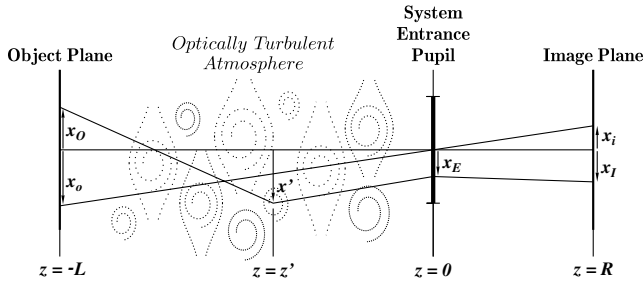


Fig. 1 Imaging scenario geometry. 2-D vectors \mathbf{x} oriented transverse to main z optical axis.

on the object plane. The main propagation axis is denoted by z ; transverse two dimensional (2-D) vectors are denoted by \mathbf{x} .

In general, light from a point $\mathbf{r}_O = (\mathbf{x}_O, -L)$ is evaluated for scatter off the ensemble of turbulent fluctuations at (\mathbf{x}', z') , passage through the aperture at $(\mathbf{x}_E, 0)$ and its effect on the light at image point (\mathbf{x}_I, R) . Each object point $(\mathbf{x}_O, -L)$ will have a reciprocal image point at $(\mathbf{x}_I, +R)$ following a chief ray through the center of the system entrance pupil. Due to the incoherent nature of the light, each photon travels independently, emitted as a quantum event, and arriving at the image plane based on conditional passage through the system entrance pupil. The instantaneous point spread function represents the electro-magnetic equivalent of the photon's quantum probability of arrival at image point \mathbf{x}_I , given the current optical turbulence pattern (considered frozen) in the region $-L < z < 0$.

2.1 Propagation Model

The Rytov approximation considers a propagating scalar wavefunction

$$U \approx U_0 \exp(\ell + i\phi), \quad (1)$$

consisting of a zeroth-order free-space solution, U_0 , plus a complex turbulence multiplier. U_0 contains the primary longitudinal phasor $\exp[ik(z+L)]$, where $i^2 = -1$ and $k = 2\pi/\lambda$ is the wavenumber, plus the phase information necessary to determine the zero-turbulence focal point of the source point in the image plane, and spherical wave phase information that will be focused by the system lens effect.

Turbulent amplitude (ℓ) and phase (ϕ) effects are imposed on the propagating wave via weak scattering from position-varying refractive index fluctuations

$$n_1(\mathbf{x}, z) = n(\mathbf{x}, z)/\langle n \rangle - 1, \quad (2)$$

where $\langle n \rangle \approx 1$ is the expectation (mean) of the refractive index $n(\mathbf{x}, z)$. Turbulent fluctuations will be modeled (exceptions noted) assuming Kolmogorov turbulence, characterized by the power spectrum²⁶

$$\Phi_n(C_n^2, \kappa) = 0.033C_n^2\kappa^{-11/3}, \quad (3)$$

where κ is the turbulent spatial frequency m^{-1} . For natural turbulence, $n_1 \ll 0.001$, such that the refractive index structure parameter, C_n^2 , is typically less than $10^{-11} \text{ m}^{-2/3}$, leading to forward scattering (in the $+z$ direction), and use of the parabolic wave equation

$$2ik\partial_z U + \nabla_{\perp}^2 U + 2k^2 n_1 U = 0, \quad (4)$$

with ∂_z the on-axis derivative operator, and ∇_{\perp}^2 the transverse Laplacian.

Using Eq. (1)'s model propagating wave, the RA method's single-scattering approximation is used to evaluate ℓ and ϕ instantaneous amplitude and phase perturbations for radiation emerging from a source at $\mathbf{r}_O = (\mathbf{x}_O, -L)$ at system entrance pupil points, $\mathbf{r}_E = (\mathbf{x}_E, 0)$,

$$\begin{bmatrix} \ell(\mathbf{r}_O; \mathbf{x}_E) \\ \phi(\mathbf{r}_O; \mathbf{x}_E) \end{bmatrix} = \begin{bmatrix} \text{Re} \\ \text{Im} \end{bmatrix} \left\{ \frac{k^2}{2\pi} \iiint_{\text{TV}} \frac{\mathcal{G}(\mathbf{r}_O; \mathbf{r}') n_1(\mathbf{r}') \mathcal{G}(\mathbf{r}'; \mathbf{r}_E) d\mathbf{r}'}{\mathcal{G}(\mathbf{r}_O; \mathbf{r}_E)} \right\}. \quad (5)$$

This equation reflects scattering from turbulence at points $\mathbf{r}' = (\mathbf{x}', z')$, $-L < z' < 0$, using free-space Green's function propagators¹⁶

$$\mathcal{G}(\mathbf{r}_1; \mathbf{r}_2) = \frac{1}{(z_2 - z_1)} \exp \left\{ ik \left[(z_2 - z_1) + \frac{|\mathbf{x}_2 - \mathbf{x}_1|^2}{2(z_2 - z_1)} \right] \right\}, \quad (6)$$

with $\mathbf{r}_i = (\mathbf{x}_i, z_i)$ and $z_2 > z_1$, to propagate the field from the source, through the scattering point, to the observation point. The Green's function in the denominator normalizes the results according to the free space effect. Note, particularly, that ℓ and ϕ are source and observation point dependent quantities; therefore they are anisoplanatic.

2.2 Modulation Transfer Function

Following the methodology of Ref. 24, we analyze the wave perturbations at the system's entrance pupil associated with the instantaneous SE MTF for the source point \mathbf{r}_O

$$\hat{M}_S(\boldsymbol{\omega}, \mathbf{r}_O) = \frac{4}{\pi} \int d\mathbf{x}_E \tilde{U}(\mathbf{r}_O; \mathbf{x}_E) \tilde{U}^*(\mathbf{r}_O; \mathbf{x}_E - D\boldsymbol{\omega}). \quad (7)$$

Here, the field variables reflect the situation just after truncation by the aperture

$$\begin{aligned} \tilde{U}(\mathbf{r}_O; \mathbf{x}_E) &= W_D(\mathbf{x}_E) \exp\{\ell(\mathbf{r}_O; \mathbf{x}_E) \\ &+ i[\phi(\mathbf{r}_O; \mathbf{x}_E) - \mathbf{a}(\mathbf{r}_O) \cdot \mathbf{x}_E]\}, \end{aligned} \quad (8)$$

and have had the mean U_0 wavefront tilt and curvature removed. The system entrance pupil is modeled using a uniformly transparent window function

$$W_D(\mathbf{x}) = \begin{cases} 1, & |\mathbf{x}| < D/2, \\ 0, & |\mathbf{x}| > D/2. \end{cases} \quad (9)$$

According to Fried's SE theory, the instantaneous turbulent phase tilt is removed, based on variable \mathbf{a} denoting the linear moment of the instantaneous phase perturbation

$$\mathbf{a}(\mathbf{r}_O) = \frac{64}{\pi D^4} \int d\mathbf{x}_E W_D(\mathbf{x}_E) \phi(\mathbf{r}_O; \mathbf{x}_E) \mathbf{x}_E. \quad (10)$$

Vector variable $\boldsymbol{\omega} = \Omega/\Omega_0$ is a normalized angular frequency, where $\Omega_0 = D/\lambda$ denotes the diffraction-limited

maximum angular frequency¹⁶ passed by a circular aperture, such that $0 < |\omega| < 1$. D is the entrance pupil diameter, dimensionalizing ω temporarily, before $\mathbf{u} = \mathbf{x}_E/D$ is used to transform integral (10) to dimensionless form.

The mean SE MTF sought is then evaluated by taking the expectation of Eq. (7), and $\omega = |\omega|$

$$M_S(\omega) = \langle \hat{M}_S(\omega, \mathbf{r}_O) \rangle = \frac{4}{\pi} \int d\mathbf{x} W_D(\mathbf{x}) W_D(\mathbf{x} - D\omega) \exp(-P_0 - P_1 - P_2 + P_3), \quad (11)$$

where the turbulent effects are expressed as the $P_0 \dots P_3$ terms. The expectation operator was passed inside the integral, as it affects only the turbulence terms. It is worth noting that this averaging process transforms the anisoplanatic instantaneous MTF into an isoplanatic second-order function, consistent with Goodman's¹⁶ analysis (pp. 395–407).

For brevity of presentation, only results are shown here, based on more complete descriptions in Refs. 20 and 24. First, amplitude and phase perturbations are considered independent, permitting the expectation of the amplitude term to be evaluated as

$$\begin{aligned} \exp(-P_0) &= \langle \exp\{\ell(\mathbf{x}) + \ell(\mathbf{x} - D\omega)\} \rangle \\ &= \exp\left\{-\frac{1}{2} \mathcal{D}_\ell(D\omega)\right\}, \end{aligned} \quad (12)$$

using \mathcal{D}_ℓ , the amplitude structure function.³¹ The remaining three terms are phase related, involving phase variance, tilt variance, and tilt-phase terms. The second term is the phase variance term, appearing as

$$\begin{aligned} \exp(-P_1) &= \langle \exp[i\phi(\mathbf{x}) - i\phi(\mathbf{x} - D\omega)] \rangle \\ &= \exp\left\{-\frac{1}{2} \mathcal{D}_\phi(D\omega)\right\}, \end{aligned} \quad (13)$$

where $\mathcal{D}_\phi(x)$ is the PSF. This term combines with $\mathcal{D}_\ell(x)$ to form the wave structure function (WSF), $\mathcal{D}(x)$, shown in path-integral form as Eq. (11) of Ref. 24. This combined term quantifies the turbulence LE effect. While the instantaneous perturbation effects were source specific (\mathbf{r}_O), therefore anisoplanatic, satisfying an energy conservation constraint,³² the second-order WSF is source independent, evaluated by weighted path integral of $C_n^2(z)$,³¹ therefore isoplanatic.

Assuming constant Kolmogorov turbulence throughout the following

$$\begin{aligned} P_0 + P_1 &= \mathcal{D}(D\omega)/2 = [\mathcal{D}_\ell(D\omega) + \mathcal{D}_\phi(D\omega)]/2 \\ &= [D\omega/(r_0/2.1)]^{5/3} = (2.1X\omega)^{5/3}, \end{aligned} \quad (14)$$

with $X = D/r_0$, using the Fried coherence diameter^{20,24}

$$r_0 = 3.018(k^2 LC_n^2)^{-3/5}. \quad (15)$$

The remaining two terms reflect SE corrections to the LE MTF (due to $P_0 + P_1$). The tilt variance term that can be written²⁴

$$P_2 = 1.0433(2.1X\omega)^{5/3} G(Q)\omega^{1/3}, \quad (16)$$

introducing parameter $Q = D/F = D/(\lambda L)^{1/2}$ to characterize diffraction influences, and function $G(Q)$ that varies from 1/2 to 1; $G \approx 1$ for $Q > 3$ ($G(Q)$ plotted in Ref. 24).

Since P_0 , P_1 , and P_2 are independent of \mathbf{x} , they do not affect the aperture integral of Eq. (11). The remaining tilt-phase correlation, written²⁴

$$P_3(\mathbf{x}, \omega) = \frac{32}{\pi D^4} \int d\mathbf{x}_a W_D(\mathbf{x}_a) [\mathbf{x}_a \cdot (D\omega)] \times [\mathcal{D}_\phi(|\mathbf{x} - D\omega - \mathbf{x}_a|) - \mathcal{D}_\phi(|\mathbf{x} - \mathbf{x}_a|)], \quad (17)$$

must be evaluated numerically. An improved version of the PSF model is introduced to facilitate evaluation of P_3

$$\begin{aligned} \mathcal{D}_\phi(Du)/2 &= \mathcal{D}(Du)\alpha(Qu)/2 \\ &= [(2.1X/Q)^{5/3}] [(Qu)^{5/3}\alpha(Qu)] \\ &= f_1(X/Q)f_2(Qu), \end{aligned} \quad (18)$$

where $u = |\mathbf{x}|/D$ is a normalized separation variable, X and Q have absorbed the D factors, and $\alpha(Qu)$ parameterizes the diffraction influence²⁴

$$\begin{aligned} \alpha(Qu) &= \int_0^1 \frac{dc}{(3/8)} \int_0^\infty d\gamma \frac{[1 - J_0(\gamma c)]}{1.118\gamma^{8/3}} \\ &\times \cos^2\left\{\gamma^2 \frac{[c(1-c)]}{4\pi(Qu)^2}\right\}, \end{aligned} \quad (19)$$

using dimensionless path ($c = z/L$) and frequency ($\gamma = Duk$) variables. Function $\alpha(Qu)$ transitions from 1/2 to 1 over eight orders of magnitude in Qu .²⁴

When turbulence is low ($X \rightarrow 0$), the turbulent exponential argument approaches zero, and the SE MTF approaches the behavior of the system MTF,

$$\begin{aligned} M_0(\omega) &= \frac{4}{\pi} \int d\mathbf{u} W_1(\mathbf{u}) W_1(\mathbf{u} - \omega); \\ &= \begin{cases} (2/\pi)[\cos^{-1}(\omega) - \omega\sqrt{1-\omega^2}], & \omega < 1, \\ 0, & \omega \geq 1, \end{cases} \end{aligned} \quad (20)$$

which depends only on ω , due to azimuthal symmetry.

When $X \neq 0$, the Eq. (11) integral was evaluated numerically using the form

$$\begin{aligned} M_T(Q, X, \omega) &= \frac{4/\pi}{M_0(\omega)} \int d\mathbf{u} W_1(\mathbf{u} - \omega) W_1(\mathbf{u}) \\ &\times \exp[+P_3(\mathbf{u}, \omega, Q, X)], \end{aligned} \quad (21)$$

where the system MTF, a function independent of Q and X , could be divided out to focus on the turbulence-varying component. In the prequel,²⁴ evaluation of M_T was handled using a relatively inefficient integration technique, but here, based on the PSF of Eq. (18), $f_1(X/Q)$ was removed from the exponential integral, allowing the remaining term

$$\begin{aligned} F_3(Q, \mathbf{u}, \omega) &= \frac{32}{\pi} \int d\mathbf{u}_a W_1(\mathbf{u}_a) [\mathbf{u}_a \cdot \hat{\mathbf{j}}\omega] \\ &\times [f_2(Q|\mathbf{u} - \hat{\mathbf{j}}\omega - \mathbf{u}_a|) - f_2(Q|\mathbf{u} - \mathbf{u}_a|)], \end{aligned} \quad (22)$$

to be tabulated and used for interpolation. The dimensionality of the tabulated results was also reduced through application of azimuthal symmetry that permitted the orientation of ω to be fixed along the y -axis (unit vector, \hat{j}).

Third, the M_T evaluations were modified to handle the impact of large $f_1(X/Q)$ effects inside the exponential through use of an offset factor A

$$M_T(Q, X, \omega) = \frac{4 \exp(A)}{\pi M_0(\omega)} \int d\mathbf{u} W_1(\mathbf{u} - \hat{j}\omega) W_1(\mathbf{u}) \times \exp[f_1(X/Q)F_3(Q, \mathbf{u}, \omega) - A]. \quad (23)$$

By adjusting A , math overflow errors in evaluating the integral could always be eliminated. Thereafter, M_T calculations could be interpreted in the form

$$M_T(Q, X, \omega) = \exp[+(2.1X)^{5/3}N(Q, X, \omega)\omega^2], \quad (24)$$

$$N(Q, X, \omega) = (2.1X)^{-5/3} \ln[M_T(Q, X, \omega)]\omega^{-2}. \quad (25)$$

Combining this term with the tilt variance effect of Eq. (16) yields the function

$$V(Q, X, \omega) = N(Q, X, \omega) - 1.0433G(Q), \quad (26)$$

such that the SE MTF can be written

$$M_S(Q, X, \omega) = M_0(\omega) \exp\{-(2.1X\omega)^{5/3} \times [1 - V(Q, X, \omega)\omega^{1/3}]\}. \quad (27)$$

Calculations of the $V(Q, X, \omega)$ function were performed for a wide range of conditions: Q from 2^{-4} to 2^{+4} by factors of 2 (9 steps), X from 10^{-1} to 10^{+3} in increments of tenths of decades (41 steps), and ω from 0.01 to 0.99 in steps of 0.01, and four additional steps at $\omega < 0.02$ (103 steps), for a database of 38,007 calculations. The analysis of this database is described in Sec. 3, using these results to formulate a new analytic SE MTF.

Sections 5 through 7 of Ref. 24 provides further details of the analysis of Fried's approach.

2.3 Range of Rytov Approximation Validity

Before examining the $V(Q, X, \omega)$ database, some discussion of the extent of validity of the Rytov method seems appropriate. Clearly, the Rytov approximation is applicable to coherent radiation studies under weak turbulence conditions, but is typically considered inappropriate for stronger turbulence scenarios, when the Rytov variance

$$\sigma_R^2 = 0.496C_n^2 k^{7/6} L^{11/6} = 0.676(X/Q)^{5/3}, \quad (28)$$

exceeds 0.5 (spherical wave coefficient used). However, in light of subsequent comparisons with Charnotskii's results^{21,26} in Sec. 4, where comparable results are achieved at Rytov variance values seemingly beyond the capability of the RA, one may question the validity of such restrictions for incoherent radiation, since temporal and spatial correlations do not exist between propagating photons.

Tatarski's analysis²⁹ only required that $n_1 \ll 1$, and that perturbation field gradients be small relative to wave number

k , conditions easily met. Similarly, Dashen³⁰ developed full and partial saturation conditions for judging RA validity, formed as ratios of a turbulence parameter, Φ_Δ , to a diffraction parameter, Ω_Δ .

For the full saturation case, Dashen used,

$$\Omega_{\Delta 1} = 6k\Lambda^2/L, \quad (29)$$

where Λ models a single scatterer scale. For a turbulent outer scale of L_o , and a spectral model³³ based on Kaimal's 1968 Kansas experiment analysis,³⁴ $\Lambda = 4.36L_o$. For the turbulence parameter, Dashen used a phase variance metric also based on an outer-scale influenced covariance

$$\Phi_{\Delta 1}^2 = k^2 L (2.309 C_n^2 L_o^{5/3}). \quad (30)$$

In this case, the RA is valid when $\Phi_{\Delta 1} < \Omega_{\Delta 1}$, or,

$$C_n^2 < 5634 L_o^{7/3} / L^3, \quad (31)$$

easily met for common outer scales of 1 m or greater.

More stringent conditions were associated with a partial saturation case involving multiple scattering scales. Dashen considered the effect of imposing a scale size cutoff that would affect both turbulent and diffraction effects. For the SE imaging problem, the most natural cutoff is the finite aperture. Dashen's Φ_Δ^2 , corresponding to an RMS phase variance, is equivalent to one of Fried's¹⁸ $\langle \Delta_j^2 \rangle$ mean aperture phase variance terms, where the order j indicates the number of phase perturbation terms corrected during the imaging process. In SE imaging, piston, tip, and tilt phase-expansion terms do not alter image quality (corresponding to Fried's order-L case), leading to the condition,

$$\Phi_{\Delta 2}^2 = \langle \Delta_L^2 \rangle = (4 \times 0.00489)(2.1X)^{5/3}, \quad (32)$$

for an aperture of diameter D . For cutoff D , Dashen's Ω_Δ parameter becomes

$$\Omega_{\Delta 2} = 12\pi Q^2. \quad (33)$$

Setting $\Phi_{\Delta 2} < \Omega_{\Delta 2}$, for a given Q , a maximum X value results

$$X_{\max}(Q) = \frac{1}{2.1} \left[\frac{36\pi^2 Q^4}{0.00489} \right]^{3/5}. \quad (34)$$

This condition translates to a maximum Rytov variance function of Q

$$\sigma_{R,\max}^2(Q) = 0.676 \left(\frac{X_{\max}}{Q} \right)^{5/3} = 14261 Q^{7/3}. \quad (35)$$

Typical terrestrial imaging scenarios involve $Q > 1/4$, implying the RA remains valid up to high-turbulence conditions.

3 Analytic Model of Short-Exposure Atmospheric Modulation Transfer Function

Using the previous section's data set, this section describes development of an analytic expression for $V(Q, X, \omega)$. This is possible due to significant correlations that exist between

$V(Q, X, \omega)$ results at different Q values. This behavior is illustrated in Fig. 2 for two sets of plots at Q values of $1/16$ and 16 , for a series of increasing values of X .

The key feature of these curves is that for moderate Q values often encountered for typical terrestrial imaging scenarios, V exceeds unity at low to moderate frequencies, resulting in enhanced behavior versus the LE response.

In developing a model of this behavior, it was first observed that $V(Q, X, 0) = V(Q, X, 1) = V_0(Q)$, permitting V to be expressed

$$V(Q, X, \omega) = V_0(Q) + V_\Delta(Q, X, \omega). \quad (36)$$

The maximum value of V (as $X \rightarrow \infty$) must also be a function of Q , $V_M(Q)$. $V_0(Q)$ and $V_M(Q)$ are plotted in Fig. 3.

Figure 3 curves both suggest asymptotic behaviors at both extremes of Q . These behaviors can be modeled using a sigmoidal function (a variant of the hyperbolic tangent)

$$\Sigma(\chi) = \frac{[\exp(\chi) - 1]}{[\exp(\chi) + 1]} = \tanh(\chi/2). \quad (37)$$

To facilitate the modeling process, a rescaled and shifted sigmoid was also introduced

$$\eta = \Sigma_S(\chi, A, B, C, D) = A + B\Sigma[C(\chi - D)]. \quad (38)$$

The center of this function occurs at $(\chi, \eta) = (D, A)$ with an overall shift of $2B$ between asymptotes, and a central derivative of $d\eta/d\chi|_{\chi=D} = BC$.

The $V_M(Q)$ function can be expressed using Σ_S as

$$V_M(Q) = \Sigma_S[\log_2(Q), 0.213, 0.072, 1.525, 0.150]. \quad (39)$$

However, $V_0(Q)$ exhibits different asymptotic behaviors at large and small Q . Therefore, a third sigmoidal form was developed, featuring a central splice (piecewise sigmoidal):

$$\Sigma_P(\chi, A, B_1, B_2, C_1, C_2, D) = \begin{cases} A + B_1\Sigma[C_1(\chi - D)], & \chi \leq D \\ A + B_2\Sigma[C_2(\chi - D)], & \chi \geq D \end{cases} \quad (40)$$

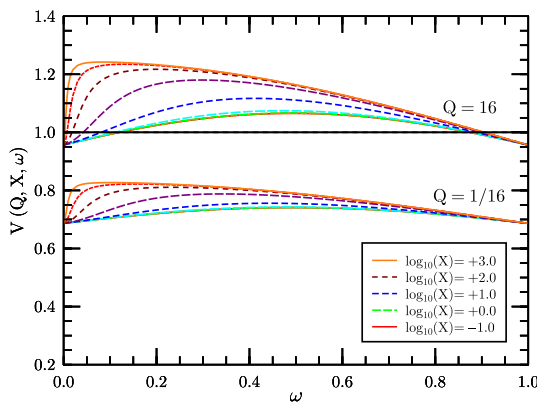


Fig. 2 Plots of $V(Q, X, \omega)$ for $Q = 1/16$ and $Q = 16$ families of curves at different X values as functions of ω .

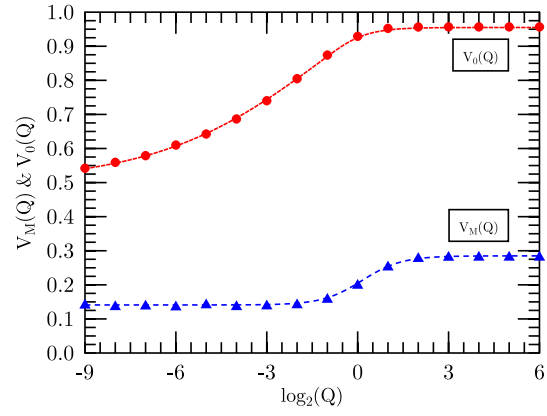


Fig. 3 Plots of $V_0(Q)$ and $V_M(Q)$ for $Q = 2^{-9} \dots 2^{+6}$.

This function is continuous in its first derivative at the splice point if $B_1C_1 = B_2C_2$. V_0 is parameterized using this function via

$$V_0(Q) = \Sigma_P[\log_2(Q), 0.870, 0.370, 0.085, 0.355, 1.545, -1.00], \quad (41)$$

where $0.370 \times 0.355 = 0.085 \times 1.545$. Equations (39) and (41) are plotted along with database derived points in Fig. 3. Variables $q = \log_2(Q)$ and $x = \log_{10}(X)$ will frequently appear hereafter as surrogates for variables Q and X in arguments to sigmoidal functions, as the majority of the modeled behaviors exhibit logarithmic dependence.

Using Eqs. (39) and (41), our problem reduces to finding an analytic expression for

$$\hat{V}_\Delta(Q, X, \omega) = V_\Delta(Q, X, \omega)/V_M(Q). \quad (42)$$

Figure 4 illustrates plots of \hat{V}_Δ for the same families of curves ($Q = 1/16$ and 16) as in Fig. 2, highlighting the similarities in behaviors at different Q values. These plots also reveal how \hat{V}_Δ develops increasingly complex behaviors as X increases.

To model these behaviors, it was observed that function curves at high ω maintained simpler forms with increasing X than at low ω , suggesting the functions could be divided at the peak and studied separately at high and low frequencies. The next step was, therefore, to model the form of the peak curves (as illustrated in Fig. 4) as functions of Q and X .

Note that the peak curves at different Q values exhibit similar X dependencies. Thus, the behaviors of the different peak curves could be modeled as shifted versions of the peak curve for $Q = 1$, described by $\omega_p(1, X)$ (abscissa) and $V_p(1, X)$ (ordinate) functions. The $Q = 1$ abscissa curve is modeled as

$$\omega_p(1, x) = \Sigma_P[x, 0.360, -0.133, -0.322, 3.450, +1.424, +1.320]. \quad (43)$$

Several $\omega_p(Q, X)$ curves at different Q levels illustrate this shifting behavior in Fig. 5. A pair of analytic expressions that approximate this behavior are given by

$$\omega_p(Q, X) = \omega_p\{Q = 1, \log_{10}(X) - x_\omega[\log_2(Q)]\}, \quad (44)$$

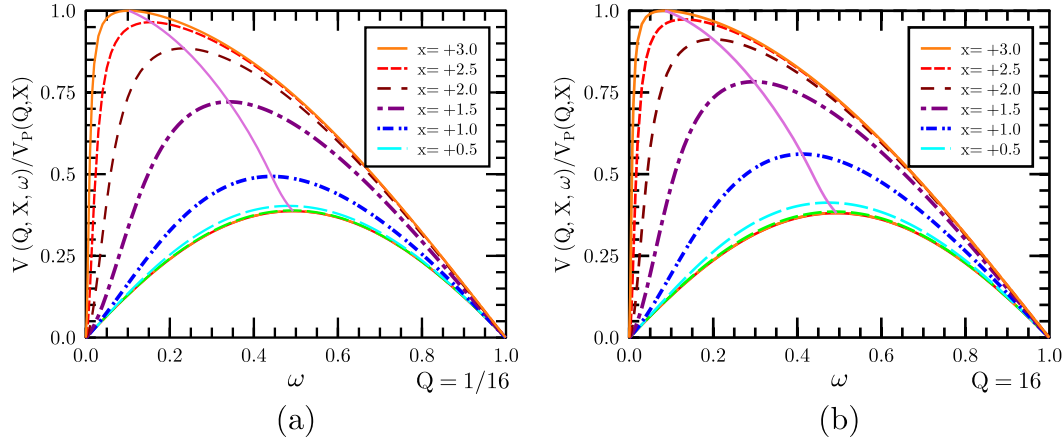


Fig. 4 Plots of $\hat{V}_\Delta = V_\Delta(Q, X, \omega)/V_M(Q)$ for $Q = 1/16$ (a) and 16 (b).

$$x_\omega(q) = \Sigma_S[q, -0.004, +0.091, +1.750, -0.050]. \quad (45)$$

Several V_P ordinate function curves, designated $V_P(Q, X) = V_\Delta(Q, X, \omega_p)$ (using the non-normalized form), are illustrated for varying X in Fig. 6, for Q values ranging from $1/16$ to 16 . This component exhibits both shifting and scaling properties, but again was quantified relative to its behavior at $Q = 1$, using

$$\begin{aligned} V_1(\mathbf{x}) &= V_P(1, 10^{\mathbf{x}}) \\ &= \Sigma_P(x, +0.122, +0.044, +0.082, \\ &\quad + 4.257, +2.300, +1.167). \end{aligned} \quad (46)$$

The behavior at $Q = 1$ was then rescaled using A_R , and shifted using x_P , in the form,

$$V_P(Q, X) = A_R[\log_2(Q)]V_1\{\log_{10}(X) - x_P[\log_2(Q)]\}, \quad (47)$$

$$A_R(q) = \Sigma_S(q, +1.051, +0.3565, +1.600, +0.150), \quad (48)$$

$$x_P(q) = \Sigma_S(q, +0.005, -0.088, +1.550, -0.150). \quad (49)$$

The function $V_P(Q, X)$ supports a further parameterization through introduction of

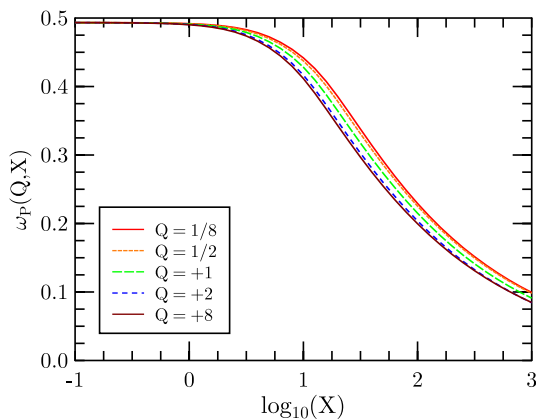


Fig. 5 Plots of $\omega_p(Q, X)$ for a range of Q values.

$$U_P(Q, X) = V_P(Q, X)/V_M(Q), \quad (50)$$

using Eqs. (47) and (39), where $0 < U_P \leq 1$. The \hat{V}_Δ curve shapes appear to vary based on height U_P , while ω dependence may be modeled using a Legendre-polynomial-related series expansion.

The Legendre polynomials begin as $P_0(z) = 1$, $P_1(z) = z$, and use recurrence relation³⁵

$$(n+1)P_{n+1}(z) = (2n+1)zP_n(z) - nP_{n-1}(z), \quad (51)$$

to characterize the interval $-1 \leq z \leq +1$. Rescaling and normalizing these functions using

$$L_n(\omega) = \sqrt{2n+1}P_n(2\omega-1), \quad (52)$$

where $z \rightarrow 2\omega - 1$, yields an orthonormal set over $0 \leq \omega \leq 1$.

Using this basis set, each \hat{V}_Δ curve could be separated into two functions at the peak position $\omega = \omega_p(Q, X)$, followed by affine transformation to stretch each monotonic function into its own ω half-range, and reverse copied to fill the opposing half-range. Thereby, two functions, each even about $\omega = 1/2$, could be analyzed using Legendre-derived basis functions. Due to their symmetry, only even-order series terms were needed to characterize each function [$L_{2n}(\omega) = L_{2n}(1-\omega)$]. The \hat{V}_Δ model could, thus,

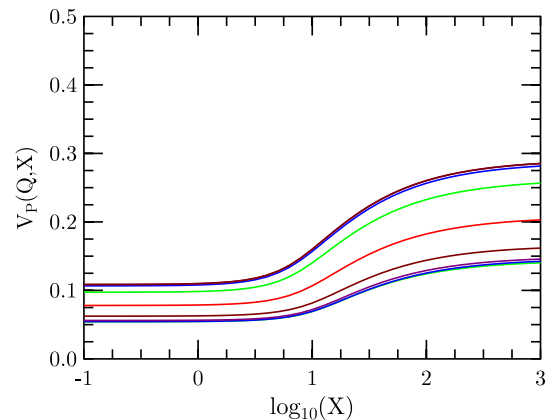


Fig. 6 Plots of $V_P(Q, X)$ for Q ranging from $1/16$ (bottom line) to 16 (top line), by factors of 2.

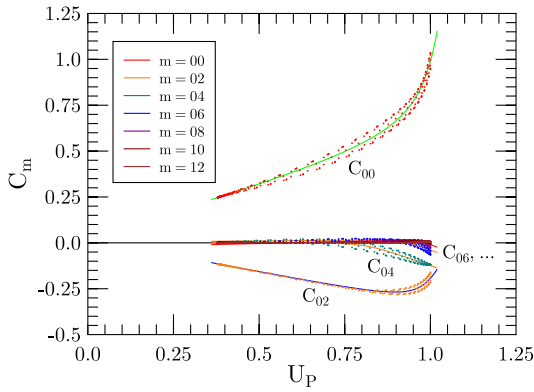


Fig. 7 Plots of $C_m(U_P)$ expansion coefficients and associated curve fits.

be splined using the coefficient sets: C_{2n} for $\omega \leq \omega_p$, and D_{2n} for $\omega \geq \omega_p$, as

$$\hat{V}_\Delta(Q, X, \omega) \approx \sum_{n=0}^{n=N} C_{2n}[U_P(Q, X)]L_{2n}\left\{\frac{\omega/2}{\omega_p(Q, X)}\right\}, \quad \omega \leq \omega_p; \quad (53)$$

$$\hat{V}_\Delta(Q, X, \omega) \approx \sum_{n=0}^{n=N} D_{2n}[U_P(Q, X)]L_{2n}\left\{1 - \frac{[1-\omega]/2}{[1-\omega_p(Q, X)]}\right\}, \quad \omega \geq \omega_p. \quad (54)$$

Sets of $C_{2n}(U_P)$ coefficient behaviors are illustrated in Fig. 7. $D_{2n}(U_P)$ behaviors are plotted in Fig. 8. Coefficients C_0 through C_8 , and D_0 , exhibit approximately hyperbolic U_P dependence. The remaining coefficients exhibit approximately linear dependence.

Hyperbolic behaviors of C_m and D_m coefficients were expressed using constants a_m through e_m in the models

$$C_m(U_P) = a_m(U_P - e_m) + b_m\sqrt{(U_P - e_m)^2 + c_m} + d_m. \quad (55)$$

Linear cases were modeled by setting $b_m = c_m = e_m = 0$. The curves plotted in Figs. 7 and 8 represent

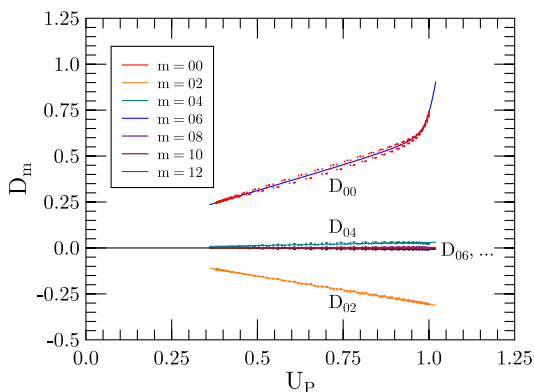


Fig. 8 Plots of $D_m(U_P)$ expansion coefficients and associated curve fits.

Table 1 SPGD hyperbolic C_m and D_m coefficients.

Coefficient	a_m	b_m	c_m	d_m	e_m
C_0	20.2124	19.6324	0.0031	0.5751	1.0686
C_2	2.1118	2.4928	0.0042	-0.3515	0.9808
C_4	-0.3413	-0.3355	0.0051	0.0051	0.7996
C_6	-0.3529	-0.3769	0.0000	0.0131	0.9041
C_8	-0.3696	-0.3982	0.0000	0.0153	0.9504
D_0	6.4372	5.8919	0.0005	0.5788	1.0341

functional fits to computed values. Fit coefficients are listed in Tables 1 and 2.

With the development of the C_m and D_m functional forms, the new analytic SE MTF model form was completed. However, given the number of free constants (80) involved, an open question remained whether a slightly modified set of coefficients could produce a better fit. To explore this possibility, a stochastic parallel gradient descent (SPGD) procedure³⁶ was applied to improve the fit to the database.

The coefficient set derived in the initial analysis (described above) was used to “seed” the SPGD optimizer. The SPGD consisted of randomly perturbing the full 80-parameter coefficient set, recomputing the RMS $V(Q, X, \omega)$ error for the full database, and comparing that error with the previous best fit error. Any new set that outperformed the prior best fit was adopted as the new best fit. Use of the SPGD reduced the overall RMS error of V from 0.006795 to 0.002728. For simplicity of presentation, coefficients listed in Tables 1 and 2 represent the SPGD best-fit coefficients. For the remaining expressions, the original results (used in the plotted figures) were retained in Eqs. (39) through (49), so curves in the various figures can be replicated. Optimized versions of these equations are given below.

To summarize, the new SE MTF model is formulated starting with the general expression in Eq. (27), then using M_0 from (20), V from (36), V_Δ from (42), expressions in Eqs. (44), (47), and (50) through (55), and results of the SPGD analysis

Table 2 SPGD linear C_m and D_m coefficients.

Coefficient	a_m	d_m
C_{10}	0.01009	-0.00452
C_{12}	0.00550	-0.00257
D_2	-0.30273	-0.00057
D_4	0.03335	-0.00413
D_6	-0.01271	0.00485
D_8	0.00425	-0.00154
D_{10}	-0.00452	0.00186
D_{12}	0.00055	-0.00019

$$V_0(Q) = \Sigma_P[q, 0.879, 0.373, 0.085, 0.373, 1.570, -0.984], \quad (56)$$

$$V_M(Q) = \Sigma_S[q, 0.221, 0.070, 1.539, 0.150], \quad (57)$$

$$\omega_P(1, X) = \Sigma_P[x, 0.351, -0.133, -0.318, +3.451, +1.407, +1.274], \quad (58)$$

$$\log_{10}[X_\omega(Q)] = \Sigma_S[q, +0.004, -0.088, +1.745, -0.050], \quad (59)$$

$$V_1(x) = V_P(1, 10^x) = \Sigma_P(x, +0.122, +0.044, +0.082, +4.296, +2.323, +1.179), \quad (60)$$

$$A_R(q) = \Sigma_S(q, +1.066, +0.352, +1.596, +0.150), \quad (61)$$

$$x_P(q) = \Sigma_S(q, -0.005, +0.089, +1.550, -0.150). \quad (62)$$

4 Comparisons with Alternative Approaches

The analytic model developed in the previous section is compared here with results obtained by Charnotskii^{21,26} and several prior analytic methods. Charnotskii²¹ used a Feynmann-path integral technique.

Figures 9 through 11 intercompare the new model with Charnotskii's²¹ Figs. 8 through 10. Charnotskii's d parameter is related to X via $X = (d^2/2)^{3/5}/2.1$, such that d values $0, \pi, 2\pi, 3\pi$, and 4π correspond to X values 0.000, 1.241, 2.851, 4.638, and 6.550, respectively. Charnotskii's N parameter is related to Q as $Q = (2N/\pi)^{1/2}$. Reported N values of the three plots were 10.0, 1.0, and 0.1, respectively, corresponding to Q values 2.523, 0.798, and 0.252. The $d = 0$ curves (the uppermost line in each graph) correspond to the system MTF, and match identically. Remaining lines in Figs. 9 and 11 were plotted using Q values that produced the closest fit to Charnotskii's results, $Q = 12.0$ in Fig. 9 and $Q = 0.02$ in Fig. 11. Lines in Fig. 10 were constructed

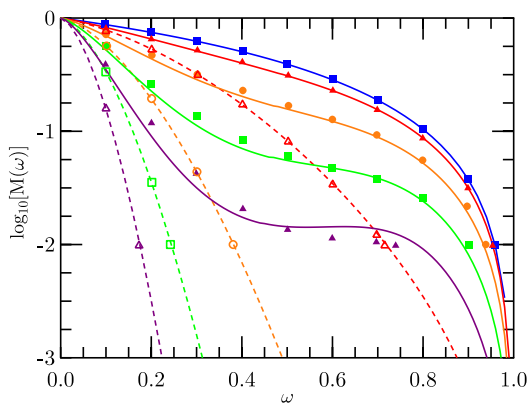


Fig. 9 Comparison of SE (solid lines) and LE (dashed lines) MTF model results using $Q = 12.0$ versus data (symbols) digitized from Ref. 21's Fig. 8.

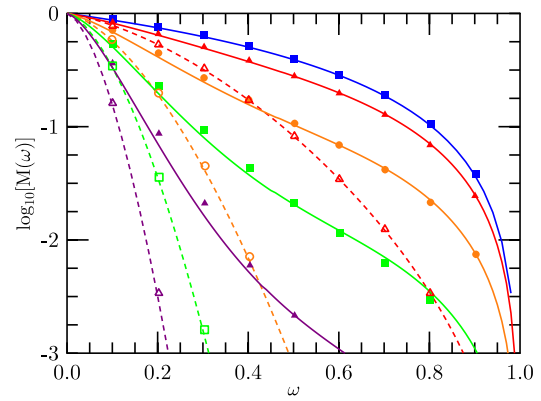


Fig. 10 Comparison of SE (solid lines) and LE (dashed lines) MTF model results using $Q = 0.798$ versus data (symbols) digitized from Ref. 21's Fig. 9.

based on the reported $N = 1$ ($Q = 0.798$). Systematic deviations employed in these plots appear consistent with Charnotskii comments that $N = 10$ and $N = 0.1$ constituted limiting cases, but might be due to approximations used when Charnotskii developed Eq. (31) of Ref. 21.

The comparisons of Figs. 9–11 provide partial verifications of both the present method and Charnotskii's calculations. A similar comparison is made in Fig. 12 between data from Fig. 2 of Ref. 26 (symbols) and simulations (lines) based on,

$$\mathcal{D}_{SA}[Q, X, r/D] = 2(2.1X)^{5/3}(r/D)^{5/3} \times \{1 - V[Q, X, (r/D)](r/D)^{1/3}\}, \quad (63)$$

an analogous SE structure function derived from the exponential kernel of Eq. (27), transformed into distances r in the entrance pupil. Results similar to Charnotskii's calculations were achieved using Q values 0.02, 0.21, 0.78, and 12.0, and $X = 0.314$ (corresponding to $d = 1.0$). Similar Q stretching as in Figs. 9 and 11 was again observed. Curiously, the lowest line (second lowest σ_R^2) exhibited the worst fit to Charnotskii's results, suggesting discrepancies between the methods are not explicable simply due to RA failure.

A key element of these results is the range of Rytov variance where similar results were obtained using RA versus the

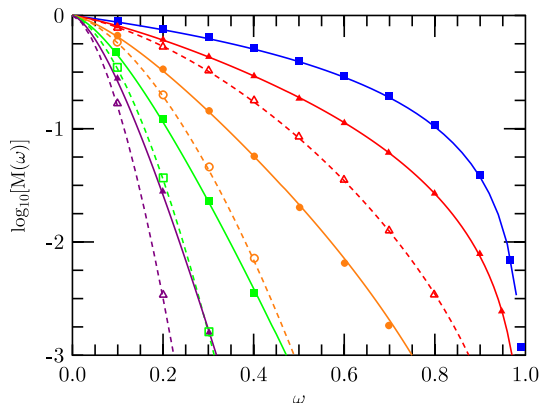


Fig. 11 Comparison of SE (solid lines) and LE (dashed lines) MTF model results using $Q = 0.02$ versus data (symbols) digitized from Ref. 21's Fig. 10.

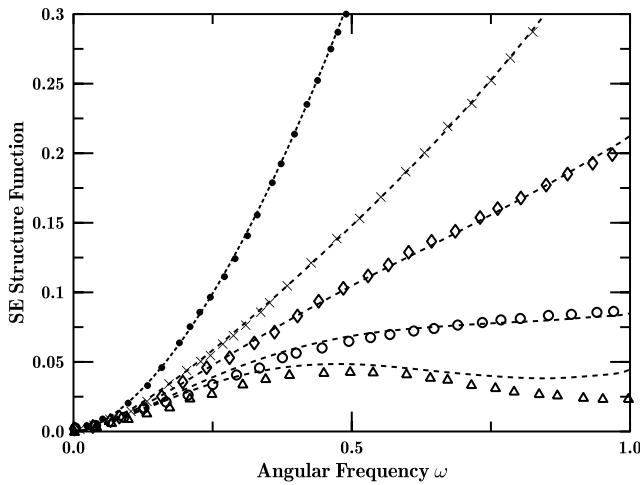


Fig. 12 Comparison of digitized data from Fig. 2 of Ref. 26 (symbols) with computed curves (dashed) using $X = 0$ (top line), and $X = 0.314$ with Q values 0.02, 0.21, 0.78, and 12.00 (bottom line).

alternative approaches of Refs. 21 and 26. While Figs. 9 and 11 involved Q stretching, a single Q adjustment appeared to correct all X cases, while no Q adjustment was used in Fig. 10 where the two strongest turbulence cases corresponded to σ_R^2 values of 12.7 and 22.8. This ability of the RA to perform at high σ_R^2 levels is consistent with the Sec. 2.3 analysis.

Lastly, four prior SE MTF models, (1) $V = 0.5$ (Fried's far-field case), (2) $V = 1.0$ (Fried's near-field case), (3) Holst's¹⁵ method where either Fried's near-field or far-field approximation was chosen based on best fit, and (4) the $V(Q, X)$ method of Ref. 24, were compared with the new analytic SE MTF model (5). An RMS metric was used to compare each estimate against database-derived MTF values, weighted by frequency ω . The RMS results computed were $E_1 = 0.035179$, $E_2 = 0.014089$, $E_3 = 0.010788$, $E_4 = 0.006431$, and $E_5 = 0.000218$. The prequel model (4) outperformed methods (1) through (3), but the new model offered dramatic improvement (by a factor of 29) over the prequel, and greater than 100 better than the far-field approach.

5 Conclusions

This paper's extended high angular frequency analysis, using the methodology described in Sec. 2, has led to a new analytic expression for the atmospheric SE MTF. This model's RMS error of 0.000218 versus numerically integrated results represents factors of 29 improvement over the prequel,²⁴ 49 over Holst,¹⁵ and 64 over Fried's near-field case.²⁰ The new model exhibits diffraction-limited behavior at all angular frequencies.

The primary focus of this effort was to provide systems performance engineers with an easily computed SE MTF that accounted for a thorough range of system and observational scenario conditions. Specifically, it improves evaluation of SE MTF degradation at high frequencies. This will aid trade studies in evaluating image reconstruction technique effectiveness where high frequency edge information losses are of critical concern.

Augmenting the present model, a previous study³⁷ showed that the new model, based on structure functions,

can treat path-varying turbulence effects, including slant-path and valley geometries. A planned future paper will expand on these results, considering the annular aperture case (Newtonian telescopes, etc.), where the circular aperture results represent the zero central obscuration limit of the more general solution.

The main caveats of the model regard the Kolmogorov spectrum used and the validity of the RA method. Regarding the spectrum, we impose the requirement that $\ell_o < D < L_o$, ensuring D occurs in the inertial subrange. Regarding the RA method, conditions derived based on Dashen's³⁰ analysis [Eqs. (31) and (35)] suggest a relatively wide range of applicability. This suitability was further tested through intercomparison with path-integral²¹ and Markov²⁶ techniques.

Results of the current study might also be used in an improved inverse filtering procedure [e.g., Ref. 5], though such a study is beyond the scope of the present work. In such a study, multiple range effects could be simulated, but special handling would be required to subsegment the images to apply different MTF's in different portions of the image field.

References

1. D. Sadot et al., "Restoration of thermal images distorted by atmosphere, using predicted atmospheric modulation transfer function," *Infrared Phys Technol.* **36**(2), 565–576 (1995).
2. D. H. Frakes, J. W. Monaco, and M. J. T. Smith, "Suppression of atmospheric turbulence in video using an adaptive control grid interpolation approach," *Proc. IEEE Int'l Conf. on Acoustics, Speech, and Sig. Proc.*, Vol. 3, pp. 1881–1884, IEEE (2001).
3. M. A. Vorontsov and G. W. Carhart, "Anisoplanatic imaging through turbulent media: image recovery by local information fusion from a set of short-exposure images," *J. Opt. Soc. Am. A* **18**(6), 1312–1324 (2001).
4. D. D. Baumgartner and B. J. Schachter, "Improving FLIR ATR performance in a turbulent atmosphere with a moving platform," *Proc. SPIE* **8391**, 839103 (2012).
5. J. Gilles and S. Osher, "Fried deconvolution," *Proc. SPIE* **8355**, 83550G (2012).
6. J. Gilles, "Mao-Gilles algorithm for turbulence stabilization," *Img. Proc. On Line* **2013**, 173–182 (2013).
7. J. Liu et al., "An efficient variational method for image restoration," *Abstr. Appl. Anal.* **2013**, 213536 (2013).
8. Y. Lou et al., "Video stabilization of atmospheric turbulence distortion," *Inverse Probl. Imag.* **7**, 839–861 (2013).
9. D. Tofsted, "Turbulence simulation: on phase and deflector screen generation," Report ARL-TR-1886, U.S. Army Research Lab. (2001).
10. G. Potvin, J. L. Forand, and D. Dion, "Some space-time statistics of the turbulent point-spread function," *J. Opt. Soc. Am. A* **24**(3), 753–763 (2007).
11. E. Repasi and R. Weiss, "Analysis of image distortions by atmospheric turbulence and computer simulation of turbulence effects," *Proc. SPIE* **6941**, 89410S (2008).
12. A. L. Robinson, J. Smith, and A. Sanders, "An efficient turbulence simulation algorithm," *Proc. SPIE* **8355**, 83550K (2012).
13. N. S. Kopeika, *A System Engineering Approach to Imaging*, SPIE Press, Bellingham, Washington (1998).
14. K. Krapels et al., "Atmospheric turbulence modulation transfer function for infrared target acquisition modeling," *Opt. Eng.* **40**(9), 1906–1913 (2001).
15. G. C. Holst, Ed., *Electro-Optical Imaging System Performance*, 3rd ed., SPIE Press, Bellingham, Washington (2002).
16. J. W. Goodman, *Statistical Optics*, J. Wiley & Sons, New York (1985).
17. M. C. Roggemann and B. Welsh, *Imaging Through Turbulence*, CRC Press, Boca Raton, FL (1996).
18. D. L. Fried, "Statistics of a geometric representation of wavefront distortion," *J. Opt. Soc. Am.* **55**(11), 1427–1435 (1965).
19. D. L. Fried, "Untitled errata for Ref. [18]," *J. Opt. Soc. Am.*, **56**(3), 410E (1966).
20. D. L. Fried, "Optical resolution through a randomly inhomogeneous medium for very long and very short exposures," *J. Opt. Soc. Am.* **56**(10), 1372–1379 (1966).
21. M. I. Charnotskii, "Anisoplanatic short-exposure imaging in turbulence," *J. Opt. Soc. Am. A* **10**(3), 492–501 (1993).
22. A. McDonald and S. C. Cain, "Parameterized blind deconvolution of laser radar imagery using an anisoplanatic optical transfer function," *Opt. Eng.* **45**(11), 116001 (2006).

23. J. R. Dunphy and J. R. Kerr, "Turbulence effects on target illumination by laser sources: phenomenological analysis and experimental results," *Appl. Opt.* **16**(5), 1345–1358 (1977).
24. D. Tofsted, "Reanalysis of turbulence effects on short-exposure passive imaging," *Opt. Eng.* **50**(1), 016001 (2011).
25. M. I. Charnotskii, "Statistics of the point spread function for imaging through turbulence," *Proc. SPIE* **8014**, 80140W (2011).
26. M. I. Charnotskii, "Statistical modeling of the point spread function for imaging through turbulence," *Opt. Eng.* **51**(10), 101706 (2012).
27. M. I. Charnotskii, "Twelve mortal sins of the turbulence propagation science," *Proc. SPIE* **8162**, 816205 (2011).
28. M. I. Charnotskii, "Common omissions and misconceptions of wave propagation in turbulence: discussion," *J. Opt. Soc. Am. A* **29**(5), 711–721 (2012).
29. V. I. Tatarski, *Wave Propagation in a Turbulent Medium*, McGraw-Hill, New York (1961).
30. D. H. Dashen, "Path integrals for waves in random media," *J. Math. Phys.* **20**(5), 139–155 (1979).
31. R. S. Lawrence and J. W. Strohbehn, "A survey of clear-air propagation effects relevant to optical communications," *Proc. IEEE* **58**(10), 1523–1545 (1970).
32. M. I. Charnotskii, "Energy conservation: a third constraint on the turbulent point spread function," *Opt. Eng.* **52**(4), 046001 (2013).
33. D. Tofsted et al., "Characterization of atmospheric turbulence during the NATO RTG-40 land field trials," *Proc. SPIE* **6551**, 65510J (2007).
34. J. C. Kaimal et al., "Spectral characteristics of surface-layer turbulence," *Q. J. Roy. Met. Soc.* **98**(417), 563–589 (1972).
35. W. Press et al., *Numerical Recipes in C*, Cambridge University Press, Cambridge, UK (1992).
36. M. Vorontsov and V. Sivokon, "Stochastic parallel gradient descent technique for high-resolution wave-front phase-distortion correction," *J. Opt. Soc. Am. A* **15**(10), 2745–2758 (1998).
37. D. Tofsted, "Short-exposure passive imaging through path-varying convective boundary layer turbulence," *Proc. SPIE* **8355**, 83550J (2012).

David H. Tofsted is a physicist with the U.S. Army Research Laboratory at White Sands Missile Range, New Mexico, with over 33 years in service. He received his BS degree in physics from Pennsylvania State University, Pennsylvania, in 1979, and MS and PhD degrees in electrical engineering from New Mexico State University, New Mexico, in 1992 and 2013. His research has focused on optical propagation problems, including numerical simulations of optical turbulence in the atmospheric boundary layer and its impacts on optical imaging systems. He has authored over 60 publications.